

Signal-SGN: A Spiking Graph Convolutional Network for Skeleton Action Recognition via Learning Temporal-Frequency Dynamics

Naichuan Zheng

Beijing University of Posts and Telecommunications
School of Information and Communication Engineering
Beijing, China
2022110134zhengnaichuan@bupt.edu.cn

Hailun Xia*

Beijing University of Posts and Telecommunications
School of Information and Communication Engineering
Beijing, China
nxiahailun@bupt.edu.cn

Yuchen Du

Beijing University of Posts and Telecommunications
School of Information and Communication Engineering
Beijing, China
duyuche@bupt.edu.cn

Zeyu Liang

Beijing University of Posts and Telecommunications
School of Information and Communication Engineering
Beijing, China
lzy_sfading@bupt.edu.cn

Abstract

For multimodal skeleton-based action recognition, Graph Convolutional Networks (GCNs) are effective models. Still, their reliance on floating-point computations leads to high energy consumption, limiting their applicability in battery-powered devices. While energy-efficient, Spiking Neural Networks (SNNs) struggle to model skeleton dynamics, leading to suboptimal solutions. We propose Signal-SGN (Spiking Graph Convolutional Network), which utilizes the temporal dimension of skeleton sequences as the spike time steps and represents features as multi-dimensional discrete stochastic signals for temporal-frequency domain feature extraction. It combines the 1D Spiking Graph Convolution (1D-SGC) module and the Frequency Spiking Convolution (FSC) module to extract features from the skeleton represented as spiking form. Additionally, the Multi-Scale Wavelet Transform Feature Fusion (MWTF) module is proposed to extract dynamic spiking features and capture frequency-specific characteristics, enhancing classification performance. Experiments across three large-scale datasets reveal Signal-SGN exceeding state-of-the-art SNN-based methods in accuracy and computational efficiency while attaining comparable performance with GCN methods and significantly reducing theoretical energy consumption.

CCS Concepts

• **Computing methodologies** → **Activity recognition and understanding.**

*Corresponding author

Permission to make digital or hard copies of all or part of this work for personal or classroom use is granted without fee provided that copies are not made or distributed for profit or commercial advantage and that copies bear this notice and the full citation on the first page. Copyrights for components of this work owned by others than the author(s) must be honored. Abstracting with credit is permitted. To copy otherwise, or republish, to post on servers or to redistribute to lists, requires prior specific permission and/or a fee. Request permissions from permissions@acm.org.
Conference'17, Washington, DC, USA

© 2025 Copyright held by the owner/author(s). Publication rights licensed to ACM.
ACM ISBN 978-x-xxxx-xxxx-x/YYYY/MM
<https://doi.org/10.1145/nnnnnnn.nnnnnnn>

Keywords

Skeleton-based Action Recognition, Spiking Neural Networks, Frequency Domain Transform

ACM Reference Format:

Naichuan Zheng, Yuchen Du, Hailun Xia, and Zeyu Liang. 2025. Signal-SGN: A Spiking Graph Convolutional Network for Skeleton Action Recognition via Learning Temporal-Frequency Dynamics. In . ACM, New York, NY, USA, 14 pages. <https://doi.org/10.1145/nnnnnnn.nnnnnnn>

1 Introduction

Multimodal skeleton-based action recognition aims to identify human actions by analyzing motion patterns from various joint-related modalities such as joints, bones, and their temporal displacements [33]. To tackle this task, numerous methods have been proposed, including CNNs [2, 3, 11, 23, 42], LSTMs [14, 20, 21], Transformers [1, 8, 24, 32], and Graph Convolutional Networks (GCNs) [7, 10, 35, 41, 44]. Among them, ST-GCN is a pioneering method that laid the foundation for GCN-based approaches [44]. Subsequent methods, such as 2s-AGCN [35] and Dynamic GCN [48], have been proposed to achieve higher accuracy in action recognition. Lightweight models like Shift-GCN [10] and CTR-GCN [7] have optimized accuracy while significantly reducing computational costs. However, these methods are all based on artificial neural networks (ANNs), which rely on floating-point operations (FLOPs), leading to significant energy consumption that limits their practicality in energy-constrained applications. Spiking Neural Networks (SNNs), regarded as third-generation neural networks, utilize spike-form features encoded as 0s and 1s to mimic neural dynamics. Unlike ANNs, SNNs process information in an event-driven manner, enabling significantly lower energy consumption while maintaining efficient computation [15]. Various SNN models have been proposed, leveraging their energy efficiency, and have been applied to a wide range of tasks, including image classification and point cloud estimation [38, 43, 46, 47, 53]. Among these, Spiking Graph Networks (SGNs) combine graph convolution with SNNs, achieving remarkable energy savings. For instance, SGNs reduce energy consumption by nearly 99% compared to vanilla GCNs [54].

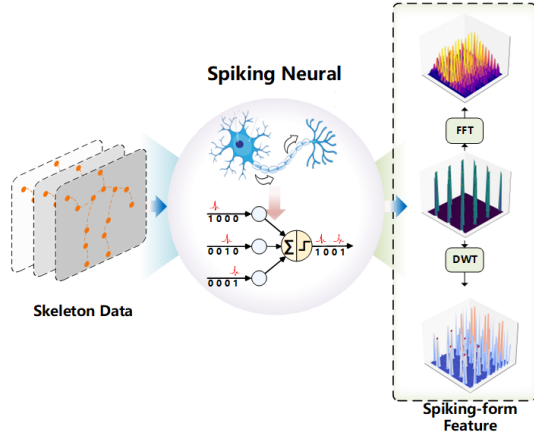


Figure 1: Motivating perspective of Signal-SGN. Skeleton data, once encoded by the spiking neural network, becomes a sparse binary representation interpretable as a multi-dimensional discrete signal. Signal-SGN leverages this perspective to apply time-frequency analysis, revealing structured spectral-temporal patterns critical for action recognition.

Specifically, SGN has been utilized for skeleton action recognition, cutting energy consumption to less than 5% of GCNs while maintaining comparable accuracy [52]. Despite its advantages, [52] treats dynamic skeleton data as static image data, artificially extending it along the spike time step dimension. This approach neglects the temporal-sensitive computational capabilities of SNNs, failing to effectively capture the inherent temporal dynamics of skeleton data. As a result, it increases computational complexity, hampers performance, and poses significant challenges for efficient training on standard deep-learning hardware. Furthermore, SGNs, like other SNN-based models [46, 47, 53], perform a simplistic Global Average Pooling (GAP) over the spike time step dimension in the task head. This naive averaging overlooks the discrete and temporal dependencies of spike-form features, impairing the model’s capacity to analyze temporal structures.

To overcome these challenges, we propose Signal-SGN for skeleton action recognition, utilizing the temporal dimension of skeleton sequences as the spiking time step and representing skeleton data as spiking-form features with multi-dimensional discrete stochastic properties, as shown in Figure 1. The architecture comprises two primary modules: a one-dimensional Spiking Graph Convolution (1D-SGC) module and a Frequency Spiking Convolution (FSC) module. The 1D-SGC extracts feature from single-frame skeleton graphs within temporal sequences and represents them as the spiking-form. Meanwhile, the FSC utilizes the Fast Fourier Transform (FFT) to transform the spiking-form features of each frame into frequency-domain and leverages complex spiking convolution for advanced feature extraction. Through successive 1D-SGC-FSC layers, the features remain discrete and aperiodic. We formulate a Multi-Scale Wavelet Transform Feature Fusion (MWTF) module to address the

limitations of simple GAP, which fails to effectively capture the temporal dynamics and frequency-specific characteristics of spiking-form features. The module leverages discrete wavelet transform (DWT) to decompose features into distinct frequency components and employs a spiking cross-attention mechanism to effectively fuse these components for robust feature representation. The proposed module significantly improves classification performance. Our main contributions can be summarized as follows:

- We propose a novel Signal-SGN network comprising multi-layer 1D-SGC-FSC that captures temporal-frequency domain spatial features of single-frame skeleton graphs and leverages the time-sensitive computational properties of SNNs to effectively model sequence-level temporal dynamics.
- We propose the MWTF module, which performs multi-scale temporal-frequency decomposition and integrates frequency-specific interactions to extract the temporal-frequency characteristics of spike-form features and enhance classification performance.
- Extensive experiments across three large-scale demonstrate that Signal-SGN surpasses State-of-the-Art (SOTA) SNN methods in terms of computational costs, and accuracy while achieving results comparable to GCN-based methods with significantly lower energy consumption.

2 Related Work

2.1 Skeleton-Based Action Recognition.

Deep learning methods have played a significant role in skeleton-based action recognition. Early approaches in this field achieved significant success using CNNs[2, 3, 11, 23, 42] and RNNs[14, 14, 20, 21]. Subsequent research has primarily focused on using Transformers[1, 8, 24, 32] and GCNs[7, 9, 10, 35, 44]. These numerous GCN-based methods typically involve nearly multi-layer stacks of Graph Convolutional Networks and Temporal Convolutional Networks. However, GCN-based networks are intrinsically tied to ANN architectures, which rely on floating-point computations. Such reliance leads to substantial energy consumption and fundamentally misaligns with practical requirements for energy-efficient solutions.

2.2 Spiking Neural Networks.

SNNs, inspired by biological neural networks, offer an energy-efficient alternative to traditional neural networks [15]. They can be implemented through two primary approaches: ANN-to-SNN conversion [16] and direct training using algorithms like STDP [6] or surrogate gradients [28]. The fundamental units, such as Leaky Integrate-and-Fire (LIF) neurons, are notable for their simplicity and biological plausibility [39]. The differential equation describes the dynamics of the LIF neuron:

$$\tau_m \frac{dV(t)}{dt} = -V(t) + R \cdot I(t), \quad (1)$$

where $V(t)$ is the membrane potential, τ_m is the time constant indicating potential decay, R is the membrane resistance, and $I(t)$ is the input current. When $V(t)$ reaches the threshold V_{th} , the neuron fires a spike and resets to V_{reset} . The LIF neuron model accurately replicates the spiking dynamics characteristic of neurons within SNNs. Inspired by ANN architectures, corresponding SNN models

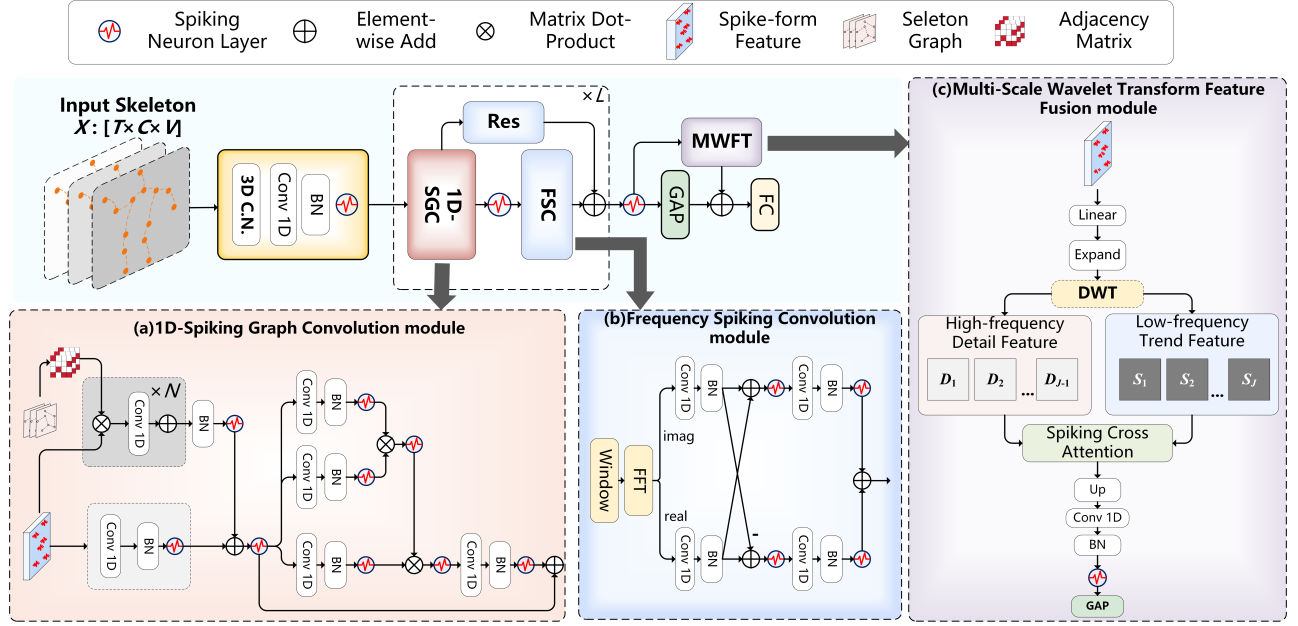


Figure 2: Overview of the proposed Signal-SGN framework for skeleton-based action recognition. The model processes skeleton sequences through four main stages: a 3D Coordinate Normalization (3D C.N.) to stabilize input representations, a 1D-Spiking Graph Convolution (1D-SGC) module to capture topological dependencies in the spiking domain, a Frequency Spiking Convolution (FSC) module that extracts frequency-aware features via FFT and complex convolution, and a Multi-Scale Wavelet Transform Feature Fusion (MWTF) module that performs multi-level decomposition and integration using discrete wavelet transform and spiking cross-attention. Final classification is conducted through global average pooling (GAP) and a fully connected (FC) layer.

have been proposed and applied to tasks such as image classification, event-driven processing, and EEG analysis [4, 5, 31]. Among these, various spiking-based Transformers have played significant roles [46, 47, 53]. Meanwhile, [52] introduces SGN for skeleton-based action recognition for the first time, achieving promising results. However, [52] treats the skeleton sequence data as static and artificially extends them along the spike time step dimension, which increases storage and computational demands. Additionally, SGNs fail to capture the discrete and non-periodic nature of spike-form features and rely on simple GAP to reduce the spike time step dimension before the classification head, limiting classification performance and accuracy.

2.3 Frequency Domain Analysis.

Frequency-domain analysis has become an increasingly important tool across various deep learning architectures for enhancing robustness and representational capacity [49]. The Fourier Transform (FT) and Wavelet Transform (WT) have been extensively adopted in CNNs for image compression and reconstruction [22], in RNNs for modeling sequential dynamics such as speech [18], and in GCNs for processing graph signals [50]. Recent work also demonstrates that adaptive frequency-based token mixing can replace costly attention mechanisms while maintaining global context modeling capabilities [37]. Moreover, in camouflaged object detection, frequency-spatial entanglement learning has proven effective in mitigating the limitations of local spatial features [36]. In the context of Vision

Transformers, frequency-guided representations have also shown to improve generalization and robustness by modulating attention with spectral priors [30].

In the context of SNNs, skeleton sequences are encoded as discrete multi-dimensional spike signals—akin to stochastic binary signals. Exploring their frequency characteristics offers promising potential for interpretable analysis and enhanced recognition. However, frequency-domain analysis for SNN-based skeleton action recognition remains underexplored and merits further attention.

3 Method

This section details the architecture of the proposed Signal-SGN, as illustrated in Figure 2. Given an input skeleton sequence, the model first applies a 3D Coordinate Normalization (3D C.N.) to standardize joint coordinates and enhance spiking encoding consistency. Then, the 1D-SGC module captures spatial dependencies of joints through spiking-based graph convolution. To further exploit frequency-domain information, FSC module transforms features via FFT and applies complex convolution for frequency-aware representation learning. Subsequently, the MWTF module decomposes spike-form features into multi-resolution frequency components using discrete wavelet transform, followed by cross-attentive fusion. The final prediction is made through GAP and a fully connected (FC) layer.

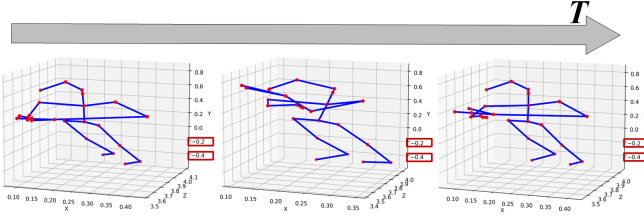


Figure 3: 3D skeleton visualization showing both positive and negative coordinate values.

3.1 3D C.N.

As shown in Figure 3, 3D skeleton data spans multiple spatial quadrants and includes both positive and negative coordinate values. This characteristic introduces challenges for SNNs, which are inherently designed for non-negative numerical inputs. In particular, the presence of negative values can disrupt rate-based spike encoding and lead to severe information loss due to binarization effects.

To address this, we apply a per-channel normalization that maps each spatial coordinate to the range $[0, 1]$. Given a skeleton sequence $X \in \mathbb{R}^{C \times T \times V}$, where $C = 3$ denotes the spatial dimensions (x, y, z), T is the number of frames, and V is the number of joints, we normalize each coordinate channel $c \in \{x, y, z\}$ independently across the full sequence utilizing:

$$c' = \frac{c - \min(c)}{\max(c) - \min(c)} \quad (2)$$

where $\min(c)$ and $\max(c)$ are computed over all joints and time steps for each coordinate channel. This process preserves the relative geometric structure while ensuring compatibility with spike-based encoding.

The normalized skeleton input is then processed by a one-dimensional convolution (Conv1D), followed by batch normalization (BN) and a spiking neuron (SN) layer. This sequence forms the initial encoding stage of Signal-SGN, and the resulting feature is denoted as X_i .

3.2 1D-SGC Module

In the 1D-SGC module, inspired by GCN, we integrate topological information by normalizing adjacency-based weights to aggregate attributes from neighboring nodes, as shown in Figure 2(a). The skeleton can be represented as a graph $\mathcal{G}(V, E)$, where the joints form a set of vertices V and the bones represent the edges E . This structure can be expressed as an adjacency matrix $A \in \mathbb{R}^{V \times V}$, where $A_{i,j} = 1$ if joints i and j are physically connected, otherwise $A_{i,j} = 0$. To incorporate topological relationships into computations, the normalized adjacency matrix S is computed as follows:

$$S = \Delta^{-\frac{1}{2}} \tilde{A} \Delta^{-\frac{1}{2}}, \quad (3)$$

where $\tilde{A} = A + I$ is the adjacency matrix with added self-connections I , and Δ is the degree matrix of \tilde{A} . This normalization ensures that the influence of each node is appropriately scaled based on its connectivity, facilitating the effective integration of topological information into the model. Subsequently, we apply Conv1d and BN along channel dimension to extract features for each skeleton

node within each spike time step, effectively aggregating features across the skeleton joints dimension.

$$G_i = \text{BN} \left[\sum_{n=0}^N \text{Conv1d} (X_i * S^n) \right], \quad (4)$$

in which S^n represents a set of matrices decomposed from S , N refers to the number of different relational matrices in the decomposition, and $*$ denotes matrix multiplication. The resulting output $G_i \in \mathbb{R}^{T \times D \times V}$, where D represents the hidden channel dimension.

To leverage the temporal dynamic characteristics of SNNs, we map the inherent temporal dimension of the features to the spike time steps of the SNNs and input the features into spiking neurons (SN). The Algorithm 1 outlines the detailed process. provided in the Appendix C.1. For compactness, we define the operation $\text{SN}[\text{BN}(\text{Conv1d}(\cdot))]$ as $\Phi(\cdot)$. The updated formula becomes:

$$G_o^{(0)} = \text{SN} (G_i) + \Phi (X_i). \quad (5)$$

Building upon the approach proposed in [53], we integrate the spike self-attention (SSA) mechanism after the graph convolution operation to enhance feature representation. The formula is as follows:

$$Q^{(0)} = \Phi_Q(G_o^{(0)}), K^{(0)} = \Phi_K(G_o^{(0)}), V^{(0)} = \Phi_V(G_o^{(0)}), \quad (6)$$

$$G^{(0)} = G_o^{(0)} + \Phi \left(Q^{(0)} K^{(0)T} V^{(0)} * s \right), \quad (7)$$

where s is the scaling factor to control the large value of the matrix multiplication result.

3.3 FSC Module

Following the 1D-SGC module, the features are re-transformed by SN into spiking-form feature—discrete, aperiodic signal sequences encoded as binary values (0s and 1s). To further extract meaningful frequency-domain feature, we propose the FSC module, as shown in Figure 2(b).

First, this module leverages a learnable window function $w_V(v) \in \mathbb{R}^V$ along the joint dimension to mitigate spectral leakage and enhance frequency analysis. Unlike fixed windows, w_V assigns adaptive weights to each joint, acting as a soft spatial gate before the frequency transform and applied element-wise to the input feature map $G^{(0)}$ as:

$$F^{(0)} = G^{(0)} \cdot w_V(v), \quad (8)$$

where $F^{(0)}$ denotes the windowed features passed to the frequency encoder, and \cdot denotes broadcasting over the joint dimension.

We perform a Fast Fourier Transform (FFT) along the joint dimension V to project the input feature $F_i^{(0)}$ into the frequency domain. The resulting complex-valued representation is separated into real and imaginary components, denoted as $F_R^{(0)}$ and $F_I^{(0)}$, which are subsequently processed by parallel branches. This transformation enables the model to extract interpretable spatial-frequency patterns across joints, facilitating enhanced action representation. To process the complex-valued FFT outputs, we propose a spiking complex convolution module that preserves and utilizes amplitude and phase information, enhancing the network's ability to capture detailed frequency-domain features:

$$F_{o,R}^{(0)} = \text{BN}[\text{Conv1d}(F_R^{(0)})], F_{o,I}^{(0)} = \text{BN}[\text{Conv1d}(F_I^{(0)})], \quad (9)$$

$$F_{o,u}^{(0)} = \text{SN} \left(F_{o,R}^{(0)} \pm_u F_{o,I}^{(0)} \right), \quad u \in \{1, 2\}. \quad (10)$$

where \pm_k represents addition (+) when $u = 1$, and subtraction (−) when $u = 2$. The fused output is then computed as:

$$F^{(0)} = \Phi \left(F_{o,1}^{(0)} \right) + \Phi \left(F_{o,2}^{(0)} \right). \quad (11)$$

The output $F^{(0)}$ represents the extracted frequency-domain features, serving as an essential input for the subsequent layers of the network. Then a complete 1D-SGC-FSC process can then be expressed as:

$$X^{(l)} = F^{(l)} + G^{(l)} + \text{res} \left(G^{(l-1)} \right) \quad (12)$$

where $X^{(l)}$ denotes the output of the l -th layer, combining the frequency-domain features $F^{(l)}$, temporal-domain features $G^{(l)}$, and a residual connection from the previous layer $\text{res} \left(G^{(l-1)} \right)$.

3.4 Multi-Scale Wavelet Transform Feature Fusion module

We formulate the MWTF module to capture the temporal dynamics and frequency-specific characteristics of spiking-form features, with its outputs fused with backbone outputs to enhance classification performance, as illustrated in Figure 2(c).

We first construct filters $\Lambda_0, \Lambda_1, \Gamma_0$, and Γ_1 based on Legendre polynomials $P_k(x)$ (details are provided in Appendix B) to decompose spiking-form features. The parameter k specifies the number of frequency coefficients extracted, influencing the spectral resolution. We apply a linear transformation to the spiking features from the final layer L of the backbone network to align the output tensor with the k coefficients, ensuring compatibility with the filters.

$$X_{\text{down}} = \text{LN} \left(\text{SN} \left(X^{(L)} \right) \right) \in \mathbb{R}^{T \times k \times V}. \quad (13)$$

To ensure compatibility with the wavelet transform, we first check whether the temporal dimension T is a power of two. If it is not, we extend the input spike-form feature X_{down} by concatenating extra frames, denoted as X_{extra} , which are duplicated copies of the beginning frames. The total number of time steps is then increased to the nearest power of two. Formally, the number of extra frames added is calculated as $2^{\lceil \log_2 T \rceil} - T$, and the final extended input becomes $\tilde{X} = [X_{\text{down}}, X_{\text{extra}}]$ along the temporal axis.

The extended input \tilde{X} is then recursively decomposed by a set of wavelet filter matrices, namely $\Lambda_0, \Lambda_1, \Gamma_0$, and Γ_1 , yielding two types of outputs at each level: detail coefficients D_j , which capture high-frequency, localized temporal features, and scaling coefficients S_j , which preserve the lower-frequency trend components, as shown in Figure 4. A complete iterative decomposition process is provided in Algorithm 2 in Appendix C.2.

To enhance the interaction between detail coefficients D_j and scaling coefficients S_j across decomposition levels j , we first up-sample them to the original temporal resolution T . Then, a spiking cross-attention mechanism is applied to capture the mutual dependencies between high-frequency and low-frequency components:

$$\hat{D}_j = \left(\Phi_Q(D_j) \cdot \Phi_K(D_j)^T \right) \Phi_V(S_j) \cdot s, \quad (14)$$

$$\hat{S}_j = \left(\Phi_Q(S_j) \cdot \Phi_K(S_j)^T \right) \Phi_V(D_j) \cdot s, \quad (15)$$

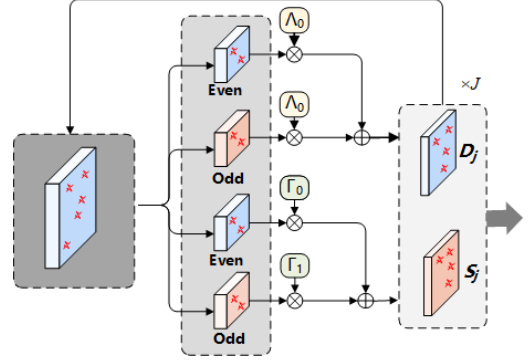


Figure 4: The process of DWT

where s is a learnable scaling factor. The scaling coefficient from the final level S_J is only upsampled (without interaction) and denoted as \hat{S}_J . All outputs $\{\hat{D}_j, \hat{S}_j\}_{j=0}^{J-1} \cup \{\hat{S}_J\}$ are aggregated and passed through spiking activation and global average pooling to yield the multi-level output:

$$\hat{X} = \text{GAP} \left(\Phi \left(\sum_{j=0}^{J-1} \hat{D}_j + \sum_{j=0}^J \hat{S}_j \right) \right). \quad (16)$$

The resulting feature \hat{X} is then fused with the SN-processed output of the final backbone layer $X^{(L)}$, and the fused representation is sent to a fully connected layer for classification:

$$\hat{y} = \text{FC} \left(\text{GAP} \left(\text{SN} \left(X^{(L)} \right) \right) + \beta \hat{X} \right), \quad (17)$$

where β is a learnable parameter balancing the contribution of temporal and spectral features. Cross-entropy loss is used for optimization during training.

4 Experiments

To demonstrate the effectiveness of Signal-SGN, we conduct skeleton-based action recognition experiments on three large-scale datasets. We compare our model against strong ANN and SNN baselines, and perform ablation studies to evaluate the contribution of each module. The following sections cover the experimental setup in detail, including dataset settings, hyperparameter configurations, comparisons with state-of-the-art methods, and ablation studies.

4.1 Dataset

NTU RGB+D [34] is a large-scale benchmark dataset for 3D human action recognition, consisting of 56,880 skeleton-based video samples from 60 action classes. Each sample contains 3D coordinates of 25 human body joints captured by the Kinect v2 sensor. We follow the standard evaluation protocols, including cross-subject (Xs)—where training and testing subjects do not overlap—and cross-view (Xv)—where training and testing samples are captured from different camera angles. NTU-RGB+D 120 [25] extends NTU 60 to 120 action categories and 114,480 video samples, with more subjects and greater view diversity. Evaluation is performed under cross-subject (Xs) and cross-setup (Xt) protocols, where the latter refers

Table 1: Comparison of Signal-SGN with prior ANN- and SNN-based models on NTU RGB+D, NTU RGB+D 120, and NW-UCLA datasets. We report classification accuracy (%), model size (Param.), computational cost (FLOPs and SOPs), and energy consumption (Power).

Model (ANN/SNN)	Param. (M)	FLOPs (G)	SOPs (G)	Power (mJ)	NTU RGB+D Xs(%)	NTU RGB+D Xv(%)	NTU RGB+D 120 Xs(%)	NTU RGB+D 120 Xt(%)	NW-UCLA (%)
Part-aware LSTM [12]	-	-	-	-	62.9	70.3	25.5	26.3	-
Spatio-Temporal LSTM [26]	-	-	-	-	61.7	75.5	55.7	57.9	-
ST-GCN [44]	3.10	3.48	-	16.01	81.5	88.3	70.7	73.2	-
2S-AGCN [35]	3.48	37.32	-	182.87	88.5	95.1	82.5	84.3	-
Shift-GCN [10]	-	10.00	-	46.00	90.7	96.5	85.3	86.6	94.6
MS-G3D [27]	3.19	48.88	-	239.51	91.5	96.2	86.9	88.4	-
CTR-GCN [7]	1.46	7.88	-	36.25	92.4	96.8	88.9	90.6	96.5
Spikformer [53]	4.78	24.07	1.69	2.17	73.9	80.1	61.7	63.7	85.4
Spike-driven Transformer [47]	4.77	23.50	1.57	1.93	73.4	80.6	62.3	64.1	83.4
Spike-driven Transformer V2 [46]	11.47	38.28	2.59	2.91	77.4	83.6	64.3	65.9	89.4
Spiking Wavelet Transformer [13]	3.24	19.30	1.48	2.01	74.7	81.2	63.5	64.7	86.7
MK-SGN [52]	2.17	7.84	0.68	0.614	78.5	85.6	67.8	69.5	92.3
Signal-SGN (Joint)	1.74	1.62	0.314	0.372	80.5	87.7	69.2	72.1	92.7
Signal-SGN (Bone+Joint)	1.74	3.24	0.628	0.744	82.5	89.2	71.3	74.2	93.1
Signal-SGN (4 ensemble)	1.74	6.48	1.28	1.488	86.1	93.1	75.3	77.9	95.9

Param. represents the model size for the network itself. For ANN methods, FLOPs, power, and accuracy are reported under standard protocols. For SNN methods, SOPs and energy estimates are computed based on spike-driven inference.

to training and testing samples being collected under different environmental and camera configurations, posing a greater challenge for model generalization. NW-UCLA [40] contains 10 action classes and 1,494 samples captured from three different viewpoints. Each sample includes 3D skeletons with 20 joints. The dataset is designed to test model robustness under cross-view scenarios.

4.2 Model Implementation and Configuration

Our model is implemented using PyTorch¹ and SpikingJelly², and all experiments are conducted on four NVIDIA V100 GPUs. The backbone network consists of 4 layers with input and output channel sizes of 3 and 64, 64 and 64, 64 and 128, 128 and 256. We use SGD optimizer with a learning rate of 0.1, decay rate of 0.1 at step 110, batch size of 64, training for 150 epochs with a dropout rate of 0.3, weight decay of 0.0001, and auxiliary loss weight ω set to 0.03.

4.3 Comparison with the State-of-the-Art

Several SOTA methods adopt multi-stream fusion strategies for improved performance [7, 10, 35]. To ensure a fair comparison, we employ the same four-stream fusion protocol in Signal-SGN, incorporating joint, bone, joint motion, and bone motion modalities. We evaluate Signal-SGN against both ANN and SNN baselines on NTU RGB+D, NTU RGB+D 120, and NW-UCLA. Classification accuracy, model size, FLOPs, synaptic operations (SOPs), and estimated energy consumption are summarized in Table 1, with calculation details provided in Appendix A. On the NTU RGB+D and NTU RGB+D 120 datasets, all sequences are downsampled to 16 frames. Compared to prior SNNs, Signal-SGN (Joint) achieves 80.5% accuracy on NTU RGB+D (Xs) while requiring only 0.372 mJ of energy—an 82.9%

reduction compared to Spikformer’s 2.17 mJ, and a 98.9% reduction compared to the ANN-based MS-G3D (239.51 mJ). Notably, our four-stream fused model further boosts accuracy to 86.1% (Xs) and 93.1% (Xv) on NTU RGB+D and 75.3% (Xs) / 77.9% (Xt) on NTU RGB+D 120, while still keeping energy usage at 1.488 mJ, which is over 96% lower than CTR-GCN (36.25 mJ) and 99.4% lower than MS-G3D. This demonstrates Signal-SGN’s superior trade-off between performance and efficiency. On the NW-UCLA, Signal-SGN achieves a competitive 95.9% accuracy, only 0.6% below CTR-GCN, while using less than 5% of its theoretical energy—further validating the model’s generalizability and low-cost design.

4.4 Ablation Studies

To evaluate the contributions of the primary components in Signal-SGN, we conducted ablation studies on the NTU-RGB+D (Xs) dataset based on joint data, with all sequences resized to 16 frames.

4.4.1 Module-wise Ablation Analysis. We first module-wise ablation analysis to evaluate the effectiveness of the proposed components in Signal-SGN. As summarized in Table 2, the base model with only the 1D-SGC module achieves 69.7% accuracy. Adding the FSC significantly boosts performance to 77.0%, indicating the advantage of incorporating frequency-domain information. Further introducing the MWTF module improves accuracy to 79.3%, demonstrating its ability to capture fine-grained temporal-frequency dynamics. A slight improvement is also observed when applying 3D coordinate normalization across different configurations, suggesting it can further stabilize input distributions and facilitate downstream spiking representation learning. Overall, these results confirm the progressive effectiveness of the proposed modules, with MWTF contributing most significantly on top of FSC.

¹<https://github.com/rwightman/pytorch-image-models>

²<https://github.com/fangwei123456/spikingjelly>

Table 2: Module-wise ablation study on NTU-RGB+D (Xs). We report model size, computational cost, and top-1 accuracy. Spikformer is included as a baseline for external comparison.

3D C.N.	1D-SGC	FSC	MWTF	Param. (M)	FLOPs / SOPs (G)	Acc (%)
Spikformer (baseline)[53]				4.78	24.07 / 1.69	73.9
-	✓	-	-	1.03	1.12 / 0.252	69.7
-	✓	✓	-	1.65	1.60 / 0.312	77.0 ^{+7.3}
-	✓	✓	✓	1.74	1.62 / 0.314	79.3 ^{+2.3}
✓	✓	-	-	1.03	1.12 / 0.252	70.5
✓	✓	✓	-	1.65	1.60 / 0.312	78.3 ^{+7.8}
✓	✓	✓	✓	1.74	1.62 / 0.314	80.5 ^{+2.2}

Table 3: Ablation study on the FSC module.

Configuration	u Interaction	Window	Acc (%)
Without FSC	-	-	70.5
Real branch only	-	Learnable	72.3 ^{+1.8}
Imaginary branch only	-	Learnable	72.1 ^{-0.2}
Real + Imag (no fusion)	-	Learnable	73.6 ^{+1.5}
Only $u = 1$ branch	$u = 1$	Learnable	75.4 ^{+1.8}
Only $u = 2$ branch	$u = 2$	Learnable	74.9 ^{-0.5}
Full FSC	$u = 1, 2$	Learnable	78.3 ^{+3.4}
Full FSC	$u = 1, 2$	Hamming	78.0 ^{-0.3}
Full FSC	$u = 1, 2$	None	77.8 ^{-0.2}

4.4.2 Ablation study on the FSC module. To validate the effectiveness of the proposed FSC module in enhancing spiking feature representation, we conduct comprehensive ablation studies, as shown in Table 3. Introducing only the real or imaginary branch improves performance from 70.5% to 72.3% and 72.1%, respectively, suggesting that both components contribute meaningfully. Combining them without interaction (u) further increases accuracy to 73.6% (+1.5%), confirming their complementarity. Enabling single interaction branches—either $u = 1$ or $u = 2$ —leads to 75.4% and 74.9%, respectively, while using both ($u = \{1, 2\}$) achieves the best performance at 78.3%, yielding a +3.4% gain over the best single-branch configuration and +7.8% over the baseline. Replacing the learnable window with a fixed Hamming window slightly reduces accuracy to 74.9%, and removing the window entirely yields 77.8%, showing the window’s limited but non-negligible contribution. These results demonstrate that the core benefit of FSC arises from complex-valued modeling and frequency-domain interaction mechanisms. To further understand the role of the learnable window, we conduct a visualization analysis across FSC layers, as detailed in Appendix D.2.

4.4.3 Qualitative Visualization of FSC module. To better understand the spiking neural behavior of our model, we visualize the joint-time ($V \times T$) spiking heatmaps from a representative “drinking water” sample, as shown in Figure 5. For each of the four FSC layers, we display activations from the real, imaginary, and fused branches, where grayscale intensity encodes the summed spike responses over the channel dimension. The fused features con-

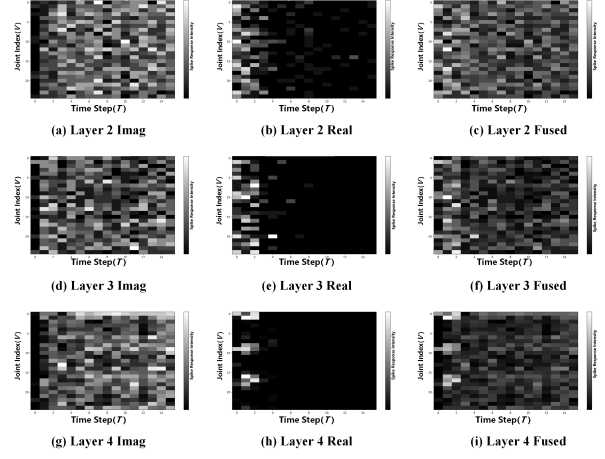


Figure 5: Spike response visualizations of FSC for the “drinking water” action sample.

Table 4: Comparison of experimental results under different MWTF settings (k and J)

MWTF	k	J	Param. (M)	FLOPs/SOPs (G)	Acc (%)
-	-	-	1.65	1.60/0.312	78.3
✓	4	1	1.68	1.61/0.313	78.9 ^{+0.6}
✓	8	1	1.73	1.62/0.314	79.8 ^{+0.9}
✓	8	2	1.74	1.62/0.315	80.3 ^{+0.5}
✓	8	3	1.74	1.62/0.317	80.5 ^{+0.2}
✓	16	3	1.83	1.64/0.320	80.5

sistently exhibit smoother and more structured spatiotemporal patterns, indicating that combining real and imaginary branches enhances feature stability and expressiveness. In contrast, the real branch shows sparser, localized firing, while the imaginary branch captures more dispersed activity. Importantly, in the final FSC layer, joints associated with the right arm—specifically the right elbow (10), wrist (11), and hand (12)—exhibit prominent activations, aligning with the expected motion of lifting a cup. Symmetric activity is also observed in joints 6–8 (left arm), reflecting bilateral arm coordination. These observations validate that FSC learns semantically meaningful joint dynamics, and that the fused representation captures discriminative patterns critical for accurate action recognition.

4.4.4 Ablation study on the MWTF module. To further analyze the effect of the MWTF module, we conduct an ablation study on its two key hyperparameters: k (number of frequency coefficients) and J (number of decomposition levels). The results, presented in Table 4, evaluate the trade-off between model complexity and classification accuracy. Starting from the baseline model without MWTF (78.3%), incorporating low-order configurations ($k=4, J=1$) leads to a modest gain (+0.6%), with the best performance (80.5%) achieved at $k=8, J=3$. This validates the importance of multi-level frequency decomposition. However, further increasing k to 16 brings no improvement, indicating saturation.

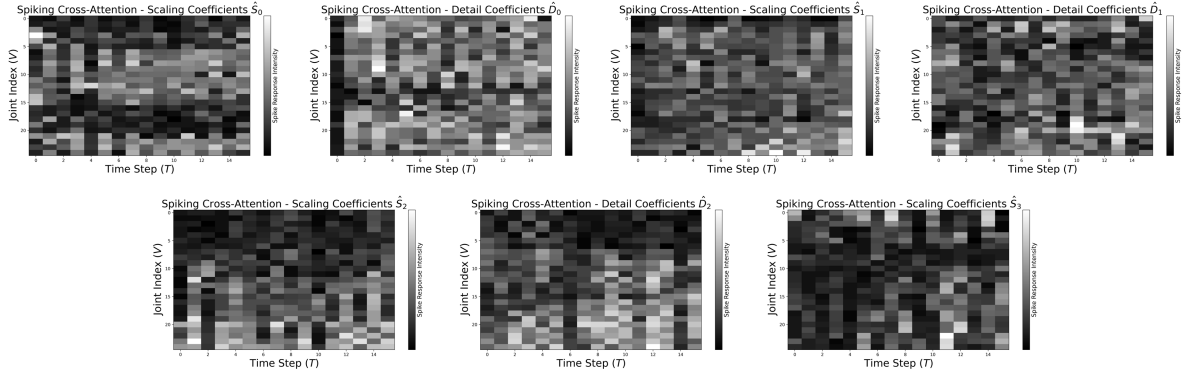


Figure 6: Visualization of upsampled detail coefficients \hat{D}_j and scaling coefficients \hat{S}_j across levels $j = 0, 1, 2$, along with the final approximation coefficient S_3 in MWTF. Each heatmap shows the spike response intensity over joints and time steps, revealing the multi-scale temporal characteristics captured by the spiking cross-attention mechanism.

Table 5: Ablation study on spiking cross-attention and inclusion of S_j in MWTF ($k=8, J=3$).

Setting	\hat{D}_j Branch	\hat{S}_j Branch	\hat{S}_J	Acc. (%)
None (Baseline)	—	—	—	78.3
Only \hat{D}_j	✓	—	—	78.9 ^{+0.6}
Only \hat{S}_j	—	✓	—	78.7 ^{-0.2}
Only S_J	—	—	✓	78.4 ^{-0.3}
$\hat{D}_j + \hat{S}_j$	✓	✓	—	79.8 ^{+0.4}
$\hat{S}_j + S_J$	—	✓	✓	79.2 ^{-0.6}
$\hat{D}_j + S_J$	✓	—	✓	79.4 ^{+0.2}
Full (Ours)	✓	✓	✓	80.5 ^{+1.3}

To further dissect MWTF’s contributions, we ablate the two spiking cross-attention branches (\hat{D}_j, \hat{S}_j) and the use of the final approximation coefficient \hat{S}_J . Results in Table 5 show that each component brings incremental benefits, with \hat{D}_j Branch alone improving performance to 78.9%, and the full configuration reaching 80.5%. To complement the analysis, we also investigate the evolution of the learnable fusion weight β training. The results, including its stabilization behavior, are provided in Appendix D.1.

4.4.5 Interpretability Analysis of MWTF via CAM Visualization. To further validate the interpretability of the MWTF module, we visualize the joint-level Class Activation Maps (CAMs) derived from its output features for three representative actions: *Drink Water*, *Stand Up*, *Reach into Pocket*, *Phone Call*, *Tear up Paper* and *Throw* (Figure 7). These CAMs highlight the spatial regions most responsive in the model’s representation. In the *Drink Water* example, high activation appears near the right wrist and elbow, matching the expected movement pattern. In *Stand Up*, the model emphasizes lower body joints, while *Reach into Pocket* shows localized attention around the hip and wrist regions. These joint-specific activations are consistent with the underlying motion characteristics of each action. The results demonstrate that MWTF’s multi-scale frequency decomposition effectively captures action-relevant joint responses, confirming

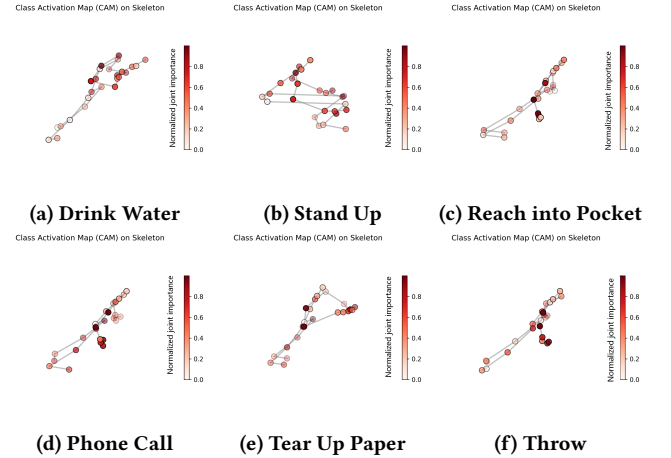


Figure 7: Class Activation Maps (CAMs) based on MWTF outputs for three representative actions. Warmer colors indicate higher joint-level importance.

the strength of time-frequency analysis in spiking skeleton-based action recognition.

4.4.6 Qualitative Visualization of Multi-Scale Coefficients. To assess the impact of multilevel decomposition and spiking cross-attention in MWTF, we visualize the upsampled detail \hat{D}_j and scaling \hat{S}_j coefficients ($j = 0, 1, 2$), along with the final approximation coefficient S_3 , for a representative *drinking water* action (Figure 6). The heatmaps reveal that \hat{D}_j emphasizes localized, high-frequency joint activations, while \hat{S}_j captures smoother, global trends. Particularly, S_3 exhibits temporally stable responses, reflecting semantic patterns preserved through hierarchical decomposition. The complementarity between \hat{D}_2 and \hat{S}_2 further demonstrates the effectiveness of spiking cross-attention in disentangling multi-scale temporal dynamics for robust recognition. A more comprehensive spectral analysis based on joint-wise frequency decomposition is provided in Appendix D.3.

5 Conclusion

We propose a novel Signal-SGN, a SNN-based framework designed to learn dynamic features in both the temporal and frequency domains for skeleton-based action recognition. The model comprises multiple stacked 1D-SGC-FSC layers, which utilize SGN to extract temporal-domain features from skeletons converted into spike forms and employ FFT and spiking complex convolution to extract frequency-domain feature. Additionally, the MWTF module, decomposes the spiking-form feature into distinct frequency components for robust feature fusion, enhancing classification performance, significantly. The final model surpasses SOTA SNNs in various aspects and achieves accuracy comparable to traditional ANN models while maintaining extremely low energy consumption, demonstrating its effectiveness and efficiency in skeleton-based action recognition.

References

- [1] Ruwen Bai, Min Li, Bo Meng, Fengfa Li, Miao Jiang, Junxing Ren, and Degang Sun. 2022. Hierarchical graph convolutional skeleton transformer for action recognition. In *2022 IEEE International Conference on Multimedia and Expo (ICME)*. IEEE, 01–06.
- [2] Carlos Caetano, François Brémond, and William Robson Schwartz. 2019. Skeleton image representation for 3d action recognition based on tree structure and reference joints. In *2019 32nd SIBGRAPI conference on graphics, patterns and images (SIBGRAPI)*. IEEE, 16–23.
- [3] Carlos Caetano, Jessica Sena, François Brémond, Jefersson A Dos Santos, and William Robson Schwartz. 2019. Skeleemotion: A new representation of skeleton joint sequences based on motion information for 3d action recognition. In *2019 16th IEEE international conference on advanced video and signal based surveillance (AVSS)*. IEEE, 1–8.
- [4] S. Cai, R. Zhang, M. Zhang, and et al. 2024. EEG-based Auditory Attention Detection with Spiking Graph Convolutional Network. *IEEE Transactions on Cognitive and Developmental Systems* (2024).
- [5] Khosla D. Cao Y., Chen Y. 2015. Spiking deep convolutional neural networks for energy-efficient object recognition. *International Journal of Computer Vision* 113 (2015), 54–66.
- [6] N. Caporale and Y. Dan. 2008. Spike timing-dependent plasticity: a Hebbian learning rule. *Annu. Rev. Neurosci.* 31, 1 (2008), 25–46.
- [7] Y. Chen, Z. Zhang, C. Yuan, and et al. 2021. Channel-wise topology refinement graph convolution for skeleton-based action recognition. In *Proceedings of the IEEE/CVF international conference on computer vision*. 13359–13368.
- [8] Yuxiao Chen, Long Zhao, Jianbo Yuan, Yu Tian, Zhaoyang Xia, Shijie Geng, Ligong Han, and Dimitris N Metaxas. 2022. Hierarchically self-supervised transformer for human skeleton representation learning. In *European Conference on Computer Vision*. Springer, 185–202.
- [9] K. Cheng, Y. Zhang, C. Cao, and et al. 2020. Decoupling gcn with dropgraph module for skeleton-based action recognition. In *Computer Vision–ECCV 2020: 16th European Conference, Glasgow, UK, August 23–28, 2020, Proceedings, Part XXIV 16*. Springer, 536–553.
- [10] K. Cheng, Y. Zhang, X. He, and et al. 2020. Skeleton-based action recognition with shift graph convolutional network. In *Proceedings of the IEEE/CVF conference on computer vision and pattern recognition*. 183–192.
- [11] Y. Du, Y. Fu, and L. Wang. 2015. Skeleton based action recognition with convolutional neural network. In *2015 3rd IAPR Asian conference on pattern recognition (ACPR)*. IEEE, 579–583.
- [12] Wang L. Du Y., Wang W. 2015. Hierarchical recurrent neural network for skeleton based action recognition. In *Proceedings of the IEEE conference on computer vision and pattern recognition*. 1110–1118.
- [13] Y. Fang, Z. Wang, L. Zhang, and et al. 2025. Spiking wavelet transformer. In *European Conference on Computer Vision*. Springer, 19–37.
- [14] Z. Gao, P. Wang, P. Lv, and et al. 2022. Focal and global spatial-temporal transformer for skeleton-based action recognition. In *Proceedings of the Asian Conference on Computer Vision*. 382–398.
- [15] Adeli H. Ghosh-Dastidar S. 2009. Spiking neural networks. *International journal of neural systems* 19, 04 (2009), 295–308.
- [16] Nguyen-Dong Ho and Ik-Joon Chang. 2021. TCL: an ANN-to-SNN conversion with trainable clipping layers. In *2021 58th ACM/IEEE Design Automation Conference (DAC)*. IEEE, 793–798.
- [17] M Horowitz. 2014. International Solid-State Circuits Conference Digest of Technical Papers.
- [18] Vercellis C. Jalayer M., Orsenigo C. 2021. Fault detection and diagnosis for rotating machinery: A model based on convolutional LSTM, Fast Fourier and continuous wavelet transforms. *Computers in Industry* 125 (2021), 103378.
- [19] Souvik Kundu, Massoud Pedram, and Peter A Beerel. 2021. Hire-snn: Harnessing the inherent robustness of energy-efficient deep spiking neural networks by training with crafted input noise. In *Proceedings of the IEEE/CVF international conference on computer vision*. 5209–5218.
- [20] Ce Li, Chunyu Xie, Baochang Zhang, Jungong Han, Xiantong Zhen, and Jie Chen. 2021. Memory attention networks for skeleton-based action recognition. *IEEE Transactions on Neural Networks and Learning Systems* 33, 9 (2021), 4800–4814.
- [21] Shuai Li, Wanqing Li, Chris Cook, Ce Zhu, and Yanbo Gao. 2018. Independently recurrent neural network (indrnn): Building a longer and deeper rnn. In *Proceedings of the IEEE conference on computer vision and pattern recognition*. 5457–5466.
- [22] S. Li, K. Xue, B. Zhu, and et al. 2020. Falcon: A fourier transform based approach for fast and secure convolutional neural network predictions. In *Proceedings of the IEEE/CVF Conference on Computer Vision and Pattern Recognition*. 8705–8714.
- [23] Yanshan Li, Rongjie Xia, Xing Liu, and Qinghua Huang. 2019. Learning shape-motion representations from geometric algebra spatio-temporal model for skeleton-based action recognition. In *2019 IEEE international conference on multimedia and Expo (ICME)*. IEEE, 1066–1071.
- [24] Haowei Liu, Yongcheng Liu, Yuxin Chen, Chunfeng Yuan, Bing Li, and Weiming Hu. 2023. TranSkeleton: Hierarchical spatial-temporal transformer for skeleton-based action recognition. *IEEE Transactions on Circuits and Systems for Video Technology* 33, 8 (2023), 4137–4148.
- [25] J. Liu, A. Shahroudy, M. Perez, and et al. 2019. Ntu rgb+ d 120: A large-scale benchmark for 3d human activity understanding. *IEEE transactions on pattern analysis and machine intelligence* 42, 10 (2019), 2684–2701.
- [26] J. Liu, A. Shahroudy, D. Xu, and G. Wang. 2016. Spatio-temporal lstm with trust gates for 3d human action recognition. In *Computer Vision–ECCV 2016: 14th European Conference, Amsterdam, The Netherlands, October 11–14, 2016, Proceedings, Part III 14*. Springer, 816–833.
- [27] Z. Liu, H. Zhang, Z. Chen, and et al. 2020. Disentangling and unifying graph convolutions for skeleton-based action recognition. In *Proceedings of the IEEE/CVF conference on computer vision and pattern recognition*. 143–152.
- [28] Zenke F. Neftci E. O., Mostafa H. 2019. Surrogate gradient learning in spiking neural networks: Bringing the power of gradient-based optimization to spiking neural networks. *IEEE Signal Processing Magazine* 36, 6 (2019), 51–63.
- [29] Priyadarshini Panda, Sai Aparna Aketi, and Kaushik Roy. 2020. Toward scalable, efficient, and accurate deep spiking neural networks with backward residual connections, stochastic softmax, and hybridization. *Frontiers in Neuroscience* 14 (2020), 653.
- [30] Badri N Patro, Vinay P Namboodiri, and Vijay Srinivas Agneeswaran. 2023. Spectformer: Frequency and attention is what you need in a vision transformer. *arXiv preprint arXiv:2304.06446* (2023).
- [31] G. Pedretti, P. Mannocci, S. Hashemkhani, and et al. 2020. A spiking recurrent neural network with phase-change memory neurons and synapses for the accelerated solution of constraint satisfaction problems. *IEEE Journal on Exploratory Solid-State Computational Devices and Circuits* 6, 1 (2020), 89–97.
- [32] C. Plizzari, M. Cannici, and M. Matteucci. 2021. Skeleton-based action recognition via spatial and temporal transformer networks. *Computer Vision and Image Understanding* 208 (2021), 103219.
- [33] B. Ren, M. Liu, R. Ding, and et al. 2024. A survey on 3d skeleton-based action recognition using learning method. *Cyborg and Bionic Systems* 5 (2024), 0100.
- [34] A. Shahroudy, J. Liu, T.-T. Ng, and et al. 2016. Ntu rgb+ d: A large scale dataset for 3d human activity analysis. In *Proceedings of the IEEE conference on computer vision and pattern recognition*. 1010–1019.
- [35] L. Shi, Y. Zhang, J. Cheng, and et al. 2019. Two-stream adaptive graph convolutional networks for skeleton-based action recognition. In *Proceedings of the IEEE/CVF conference on computer vision and pattern recognition*. 12026–12035.
- [36] Yanguang Sun, Chunyan Xu, Jian Yang, Hanyu Xuan, and Lei Luo. 2024. Frequency-spatial entanglement learning for camouflaged object detection. In *European Conference on Computer Vision*. Springer, 343–360.
- [37] Yuki Tatsunami and Masato Taki. 2024. Fft-based dynamic token mixer for vision. In *Proceedings of the AAAI Conference on Artificial Intelligence*, Vol. 38. 15328–15336.
- [38] A. Tavanaei, M. Ghodrati, S. R. Kheradpisheh, and et al. 2019. Deep learning in spiking neural networks. *Neural networks* 111 (2019), 47–63.
- [39] C. Teeter, R. Iyer, V. Menon, and et al. 2018. Generalized leaky integrate-and-fire models classify multiple neuron types. *Nature communications* 9, 1 (2018), 709.
- [40] J. Wang, X. Nie, Y. Xia, and et al. 2014. Cross-view action modeling, learning and recognition. In *Proceedings of the IEEE conference on computer vision and pattern recognition*. 2649–2656.
- [41] Xuanhan Wang, Yan Dai, Lianli Gao, and Jingkuan Song. 2022. Skeleton-based action recognition via adaptive cross-form learning. In *Proceedings of the 30th ACM International Conference on Multimedia*. 1670–1678.
- [42] Yangyang Xu, Jun Cheng, Lei Wang, Haiying Xia, Feng Liu, and Dapeng Tao. 2018. Ensemble one-dimensional convolution neural networks for skeleton-based action recognition. *IEEE Signal Processing Letters* 25, 7 (2018), 1044–1048.
- [43] K. Yamazaki, V.-K. Vo-Ho, D. Bulsara, and et al. 2022. Spiking neural networks and their applications: A review. *Brain Sciences* 12, 7 (2022), 863.

- [44] S. Yan, Y. Xiong, and D. Lin. 2018. Spatial temporal graph convolutional networks for skeleton-based action recognition. In *Proceedings of the AAAI Conference on Artificial Intelligence*, Vol. 32.
- [45] Man Yao, Huanhuan Gao, Guangshe Zhao, Dingheng Wang, Yihan Lin, Zhaoxu Yang, and Guoqi Li. 2021. Temporal-wise attention spiking neural networks for event streams classification. In *Proceedings of the IEEE/CVF international conference on computer vision*. 10221–10230.
- [46] M. Yao, J. Hu, T. Hu, and et al. 2024. Spike-driven transformer v2: Meta spiking neural network architecture inspiring the design of next-generation neuromorphic chips. *arXiv preprint arXiv:2404.03663* (2024).
- [47] M. Yao, J. Hu, Z. Zhou, and et al. 2024. Spike-driven transformer. *Advances in neural information processing systems* 36 (2024).
- [48] F. Ye, S. Pu, Q. Zhong, and et al. 2020. Dynamic gcn: Context-enriched topology learning for skeleton-based action recognition. In *Proceedings of the 28th ACM international conference on multimedia*. 55–63.
- [49] Kun Yi, Qi Zhang, Longbing Cao, Shoujin Wang, Guodong Long, Liang Hu, Hui He, Zhendong Niu, Wei Fan, and Hui Xiong. 2023. A survey on deep learning based time series analysis with frequency transformation. *arXiv preprint arXiv:2302.02173* (2023).
- [50] W. Yu and Z. Qin. 2020. Graph convolutional network for recommendation with low-pass collaborative filters. In *International Conference on Machine Learning*. PMLR, 10936–10945.
- [51] Hanle Zheng, Yujie Wu, Lei Deng, Yifan Hu, and Guoqi Li. 2021. Going deeper with directly-trained larger spiking neural networks. In *Proceedings of the AAAI conference on artificial intelligence*, Vol. 35. 11062–11070.
- [52] N. Zheng, H. Xia, and Z. Liang. 2024. MK-SGN: A Spiking Graph Convolutional Network with Multimodal Fusion and Knowledge Distillation for Skeleton-based Action Recognition. *arXiv preprint arXiv:2404.10210* (2024).
- [53] Z. Zhou, Y. Zhu, C. He, and et al. 2022. Spikformer: When spiking neural network meets transformer. *arXiv preprint arXiv:2209.15425* (2022).
- [54] Z. Zhu, J. Peng, J. Li, and et al. 2022. Spiking graph convolutional networks. *arXiv preprint arXiv:2205.02767* (2022).

In the appendix, we first provide a supplemental detailed description of Power Consumption, Legendre Polynomial-Based Filters, Algorithm and Supplementary Analysis.

A Power Consumption

We assume that multiply-and-accumulate (MAC) and accumulate (AC) operations are implemented on the 45 nm technology node with $E_{MAC} = 4.6$ pJ and $E_{AC} = 0.9$ pJ [17]. The FLOPs for Signal-SGN and all reproduced models are calculated using FVCore³, providing accurate estimates for each model component. These FLOPs are then combined with the firing rate and spike time steps to compute SOPs as:

$$SOPs(l) = fr \times T \times FLOPs(l), \quad (18)$$

where fr is firing rate, T is the spike time steps, $FLOPs(l)$ refers to the floating-point operations of l , defined as the number of MAC operations performed in l block or layer, and SOPs are the number of spike-based AC operations.

The model's theoretical energy consumption is described as, according to [19, 29, 38, 45, 51, 53]:

$$E_{\text{Signal-SGN}} = E_{EAC} \times FL_{\text{SNN Conv}}^i + E_{AC} \times \left[\left(\sum_{n=\tilde{n}}^N SOP_{\text{SNN Conv}}^n + \sum_{m=1}^M SOP_{\text{SNN FC}}^m + \sum_{l=1}^L SOP_{\text{SNN SSA}}^l + \sum_{f=1}^F SOP_{\text{SNN FFT}}^f \right) + SOP_{\text{SNN MWTF}} \right] \quad (19)$$

where $FL_{\text{SNN Conv}}^i$ is the first layer to encode skeleton into spike-form. Then the SOPs of N SNN Conv layers, M SNN Fully Connected Layer (FC), L SSA layer, F FFT layer and MWTF are added together and multiplied by E_{AC} . The theoretical energy consumption for ANN and SNN models is calculated as follows:

For ANNs, the energy consumption of a block b is given by:

$$\text{Power}(b) = E_{EAC} \times FLOPs(b). \quad (20)$$

For SNNs, the energy consumption of a block b is given by:

$$\text{Power}(b) = E_{AC} \times SOPs(b). \quad (21)$$

B Legendre Polynomial-Based Filters

Legendre polynomials $P_k(x)$, defined over the interval $[-1, 1]$, provide a robust orthogonal basis for constructing frequency-domain filters aimed at decomposing spike-like features in temporal signals. Their orthogonality condition ensures that different polynomial orders yield mutually independent basis functions. The polynomials are generated recursively using the relation:

$$\begin{aligned} P_0(x) &= 1, \quad P_1(x) = x, \\ (k+1)P_{k+1}(x) &= (2k+1)xP_k(x) - kP_{k-1}(x). \end{aligned} \quad (22)$$

Their orthogonality condition, as:

$$\int_{-1}^1 P_m(x)P_n(x) dx = \frac{2}{2n+1} \delta_{mn} \quad (23)$$

This property is particularly advantageous for designing a set of filters that can isolate specific frequency components with minimal interference.

To apply these polynomials to temporal-domain signals sampled over $[0, T]$, we first normalize the time index:

$$u = \frac{t}{T}, \quad u \in [0, 1]. \quad (24)$$

We then map $[0, 1]$ to $[-1, 1]$:

$$x = 2u - 1. \quad (25)$$

This transformation aligns the original time domain with the canonical domain of the Legendre polynomials, ensuring straightforward evaluation of $P_k(x)$ at the corresponding sampling points.

Within this framework, low-frequency ("low-pass") filters are derived from lower-order Legendre polynomials, which vary slowly across $[-1, 1]$. To ensure proper normalization, each polynomial is scaled by $\sqrt{2k+1}$. Introducing a half-period shift $\Delta = 0.5$ in the normalized time domain allows us to construct two distinct low-pass filters by evaluating the polynomials at slightly different points. Specifically, the low-pass filters are defined as:

$$\Lambda_0[k, t] = \sqrt{2k+1} P_k(2u - 1), \quad (26)$$

$$\Lambda_1[k, t] = \sqrt{2k+1} P_k(2(u + 0.5) - 1) = \sqrt{2k+1} P_k(2u). \quad (27)$$

Here, $\Lambda_0[k, t]$ and $\Lambda_1[k, t]$ share the same polynomial family but are evaluated at $2u - 1$ and $2u$, respectively, introducing a phase-like shift that distinguishes the two filters in their temporal and spectral responses.

For high-frequency ("high-pass") filters, the ideal construction involves deriving them from multi-resolution analysis (MRA) conditions to ensure orthogonality and perfect reconstruction. Nonetheless, a representative scheme, consistent with the normalization above, is given by:

$$\Gamma_0[k, t] = \sqrt{2} \Lambda_0[k, t], \quad (28)$$

$$\Gamma_1[k, t] = \sqrt{2} \Lambda_1[k, t]. \quad (29)$$

Taken together, these four filters ($\Lambda_0, \Lambda_1, \Gamma_0, \Gamma_1$) can decompose the signal into distinct frequency bands, enabling a nuanced analysis of spike-like features. By carefully mapping temporal samples into the Legendre polynomial domain, employing a normalized and shifted set of low-pass filters, and incorporating a high-pass counterpart, this approach provides a stable, orthogonal, and frequency-selective analytical framework. This framework facilitates effective characterization, improved interpretability, and subsequent analyses of temporal-varying signals in a multi-resolution context.

C Algorithm

This section presents the essential pseudocode and detail description underpinning the computational framework discussed in this work.

C.1 Spiking Neuron Dynamics Simulation

The Spiking Neuron Dynamics describes the core mechanisms governing the temporal dynamics of spiking neurons within the network, outlined in Algorithm 1.

The input, $G \in \mathbb{R}^{T \times D \times V}$, represents the temporal sequence of feature maps for T time steps, where D and V denote the feature

³<https://github.com/facebookresearch/fvcore>

Algorithm 1 Spiking Neuron Dynamics Simulation

```

1: Input:  $G \in \mathbb{R}^{T \times D \times V}$ 
2: Parameters:  $\tau, V_{\text{rest}}, R, V_{\text{th}}$ 
3: Output:  $G_o \in \mathbb{R}^{T \times C \times V}$ 
4: Initialize  $V(t)$  and  $G_o$ 
5: for  $t = 0$  to  $T - 1$  do
6:    $G_i(t) \leftarrow G[t, :, :]$ 
7:    $\tau \frac{dV(t)}{dt} \leftarrow -(V(t) - V_{\text{rest}}) + R \cdot G_i(t)$ 
8:   if  $V(t) \geq V_{\text{th}}$  then
9:      $G_o[t, :, :] \leftarrow 1$ 
10:     $V(t) \leftarrow V_{\text{rest}}$  {Reset voltage after spike}
11:   else
12:      $G_o[t, :, :] \leftarrow 0$ 
13:   end if
14: end for
15: return  $G_o \in \mathbb{R}^{T \times D \times V}$ 

```

dimension and the number of vertices (e.g., joints in skeleton data), respectively. The algorithm computes the output $G_o \in \mathbb{R}^{T \times C \times V}$, which represents the spike emissions over time, with C corresponding to the output channel dimension.

At each time step t , the membrane potential $V(t)$ is updated based on the input current $G_i(t)$ and the parameters governing spiking neuron dynamics, including the membrane time constant τ , the resting potential V_{rest} , the resistance R , and the firing threshold V_{th} . Specifically, the potential evolves according to the equation:

$$\tau \frac{dV(t)}{dt} = -(V(t) - V_{\text{rest}}) + R \cdot G_i(t), \quad (30)$$

where $G_i(t) = G[t, :, :]$ is the input tensor for time step t . If the membrane potential $V(t)$ exceeds the threshold V_{th} , a spike is emitted ($G_o[t, :, :] = 1$), and the potential is reset to V_{rest} . Otherwise, no spike is generated ($G_o[t, :, :] = 0$).

This mechanism enables the simulation of spike-based information transmission, where G_o captures the spiking behavior at each time step. The tensor G_o has the same temporal and spatial resolution as the input but reflects the binary spike activations, effectively encoding temporal dynamics into discrete spike events.

The iterative process ensures that spiking neurons dynamically respond to varying inputs while adhering to biologically inspired principles. Subsequent layers of spiking neurons follow similar dynamics, allowing the network to propagate spike-based representations through deeper processing stages.

C.2 Iterative Decomposition

The Iterative Decomposition algorithm describes the process of decomposing spike-form features into their frequency domain representations. This hierarchical decomposition enables the separation of temporal dynamics into high-frequency detail coefficients and low-frequency scaling coefficients, which are critical for efficient feature extraction and multi-resolution analysis in SNNs.

The iterative decomposition process begins with the extended spike-form feature tensor \tilde{X} , which serves as the initial input. The tensor is initialized as X_0 , providing the starting representation for decomposition across J levels.

Algorithm 2 Iterative Decomposition

```

1:  $\tilde{X}_0 \leftarrow \tilde{X}$ 
2: for  $j = 0$  to  $J - 1$  do
3:    $X_{\text{even}}^{(j)} \leftarrow \tilde{X}_j[:, 2, :, :]$ 
4:    $X_{\text{odd}}^{(j)} \leftarrow \tilde{X}_j[1 :: 2, :, :]$ 
5:    $D_j \leftarrow \Gamma_0 \cdot X_{\text{even}}^{(j)} + \Gamma_1 \cdot X_{\text{odd}}^{(j)}$ 
6:    $S_j \leftarrow \Lambda_0 \cdot X_{\text{even}}^{(j)} + \Lambda_1 \cdot X_{\text{odd}}^{(j)}$ 
7:    $\tilde{X}_{j+1} \leftarrow S_j$ 
8: end for
9:  $S_J \leftarrow \tilde{X}_J$ 
10: return  $\{D_j\}_{j=0}^{J-1}$  and  $\{S_j\}_{j=0}^J$ 

```

At each decomposition level j , the input tensor X_j is divided along its temporal dimension into even and odd indexed components, denoted as $X_{\text{even}}^{(j)}$ and $X_{\text{odd}}^{(j)}$, respectively. These components are independently processed to compute the detail coefficients D_j and scaling coefficients S_j as follows:

$$D_j = \Gamma_0 \cdot X_{\text{even}}^{(j)} + \Gamma_1 \cdot X_{\text{odd}}^{(j)}, \quad (31)$$

$$S_j = \Lambda_0 \cdot X_{\text{even}}^{(j)} + \Lambda_1 \cdot X_{\text{odd}}^{(j)}. \quad (32)$$

where, Γ_0, Γ_1 are high-pass filter matrices used to extract the detail coefficients D_j , which capture high-frequency temporal variations. Conversely, Λ_0, Λ_1 are low-pass filter matrices that compute the scaling coefficients S_j , preserving the low-frequency temporal information.

After computing D_j , the scaling coefficients S_j are propagated to the next level by setting $X_{j+1} = S_j$. This iterative decomposition continues across all J levels, refining the temporal representation at each step. Upon completing the J -th level, the final scaling coefficients S_J are obtained. The process outputs the set of detail coefficients $\{D_j\}_{j=0}^{J-1}$ and scaling coefficients $\{S_j\}_{j=0}^J$, providing a hierarchical representation of the temporal dynamics.

Upon completion, the algorithm outputs a set of detail coefficients $\{D_j\}_{j=0}^{J-1}$ and the final scaling coefficients S_J , collectively encapsulating the hierarchical temporal structure of the input. The complete iterative decomposition process is outlined in Algorithm 2, providing a systematic and computationally efficient method for processing spike-form feature.

D Supplementary Analysis

D.1 Analysis of Window function

To analyze the role of the learnable joint-wise window function $w_V(v)$, we visualize its values across all FSC layers at both the beginning and end of training, as shown in Figure 8. Initially, all layers exhibit near-zero or uniform weights, especially in deeper layers like Layer 4, where the window is almost flat and close to zero, as shown in Figure 8a. This indicates that the network starts without any strong spatial preference in the frequency modulation stage.

After training, however, the learned windows evolve into highly diverse and non-uniform patterns across joints, as shown in Figure 8b. The early layers (e.g., Layer 1) show sharp variations, possibly

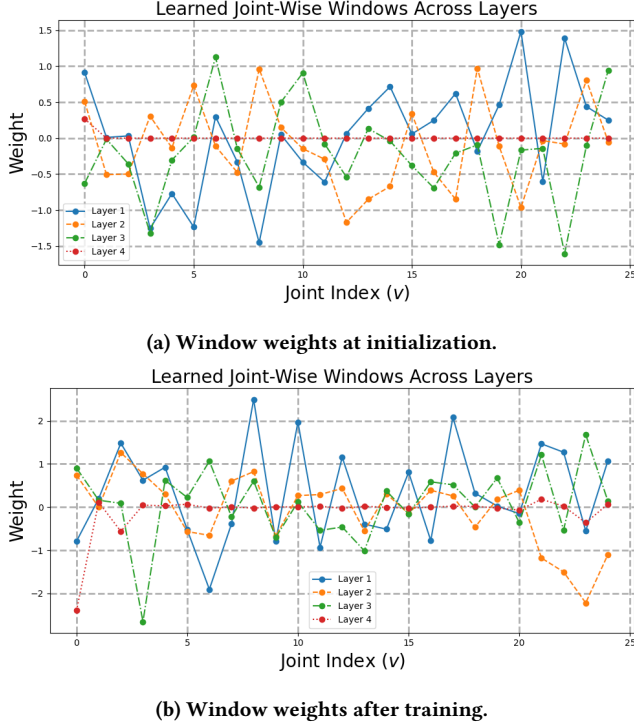


Figure 8: Visualization of the learned joint-wise window functions $w_V(v)$ across FSC layers.



Figure 9: Joint evolution of training loss and the learnable fusion weight β .

focusing on localized joints, while deeper layers develop smoother yet still distinctive profiles. This progression suggests that learning a fully adaptive window function allows the network to emphasize or suppress specific joints based on spatiotemporal dynamics, with joint-wise spectral weighting acting as a spatial prior to guide frequency decomposition according to human motion structure and semantics.

D.2 Analysis of Learnable Fusion Parameter β

To complement the ablation study on the MWTF module, we provide an analysis of the learnable fusion weight β in the final classification stage, as defined in Equation (17). Figure 9 illustrates the joint evolution of the training loss and the value of β throughout training. We observe that β fluctuates significantly during the initial 20 epochs, reflecting the model's attempt to dynamically balance the temporal backbone output and the spectral feature \hat{X} extracted by MWTF. As the training loss steadily declines, β gradually stabilizes. By the end of training, β converges to approximately 0.42, indicating that the model assigns moderate but consistent weight to the spectral branch. This behavior suggests that while the primary classification signal originates from the SN-processed temporal pathway, the MWTF-derived spectral features provide substantial complementary information. The learnable fusion mechanism, governed by β , thus plays a key role in adaptively integrating multiscale dynamics for robust action recognition.

D.3 Frequency-Domain Analysis of MWTF

To further interpret the effectiveness of the proposed spiking cross-attention fusion across wavelet decomposition levels, we perform a joint-wise spectral analysis using the example of the "drinking water" action on NTU-RGB+D. As shown in Figure 10, each subfigure presents the magnitude spectrogram obtained from the FFT of a single channel with the highest temporal variance.

The final cross-attentively fused output \hat{X} in Figure 10(a) exhibits an enriched spectrum that combines both low- and high-frequency components. Compared to the low-frequency-dominated baseline $X^{(L)}$ in Figure 10(b), \hat{X} demonstrates enhanced high-frequency responses particularly at joints 6 (right shoulder), 8 (right elbow), 10 (right wrist), and 12 (right hand), which are anatomically responsible for raising the arm and bringing the hand to the mouth during drinking.

Figures 10(c)–(f) illustrate the spiking cross-attentively fused detail coefficients \hat{D}_0 to \hat{D}_3 , representing progressively higher frequency bands as the decomposition level increases. Specifically, \hat{D}_0 and \hat{D}_1 capture mid-frequency activations in joints 6, 8, and 10, reflecting shoulder and elbow articulation during arm lifting. The component \hat{D}_2 highlights more localized and rapid changes in joints 10 and 12, aligning with the wrist-to-mouth trajectory. As the final decomposition level, \hat{D}_3 is generated via upsampling of the residual high-frequency component and retains only coarse responses—mainly from trunk-related joints (e.g., joints 2 and 3)—representing global pose adjustments.

Figures 10(g)–(i) show the corresponding scaling coefficients \hat{S}_0 to \hat{S}_2 , also fused through spiking cross-attention (cf. Eq. 15). These components preserve low-frequency temporal dynamics and body stability. For example, \hat{S}_1 and \hat{S}_2 maintain dominant low-frequency energy at joints 2 (chest) and 3 (neck), which are critical for torso alignment and posture maintenance during the action.

Overall, this frequency-domain decomposition provides fine-grained interpretability of motion dynamics across joint hierarchies and temporal scales, confirming that the proposed spiking cross-attention fusion mechanism effectively preserves both semantic structure and dynamic variations by adaptively emphasizing functionally critical joints in the spectral domain.

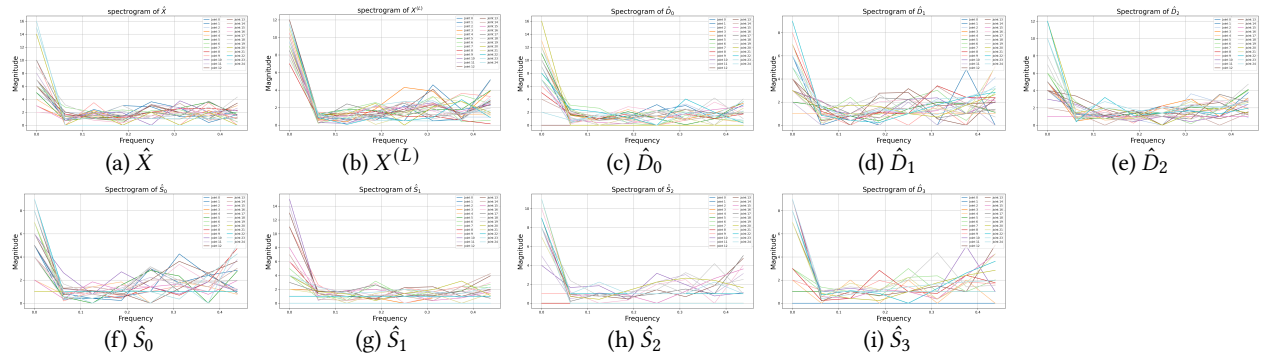


Figure 10: Joint-wise frequency spectrograms of multiscale components, based on the "drinking water" action. Each plot shows the FFT magnitude curves of all 25 joints, revealing their spectral activity at various decomposition levels.